Eur. Phys. J. Plus (2022) 137:564
https://doi.org/10.1140/epjp/s13360-022-02759-8

THE EUROPEAN PHYSICAL JOURNAL PLUS

Regular Article

An experimental study of the pattern formation in forced surface waves

Reda Guedifa[1,a], **Madjid Hachemi**[2,b]

[1] Dynamic Motors and Vibroacoustic Laboratory, Faculty of Technology, University of Boumerdes, Boumerdes, Algeria
[2] Laboratory Energetics Mechanics and Engineering, Faculty of Technology, University of Boumerdes, Boumerdes, Algeria

Received: 25 November 2021 / Accepted: 21 April 2022

Abstract Pattern formation in forced surface waves occurs between two layers of immiscible fluids of different densities, in which a vertical vibration is imposed, leading to stationary waves. This experimental study focuses primarily on the formation of the various wave patterns (solitary waves and meniscus waves) and the onset of Faraday waves. Three control parameters are varied to produce different flow patterns: the forcing amplitude and frequency as well as the depth (A_f, ω_f, Γ). In this paper, we investigate low forcing frequencies ranging from 3 to 5 Hz, and high forcing amplitudes ranging from 3 to 15 mm. The measured responses correspond to the oscillation frequencies of the free surface ω_s and their associated wavelength λ_s. It is found that a succession of equilibrium states occurs spatially periodic structures and symmetric up to well-defined thresholds. Beyond these thresholds, symmetrical structures are broken and may follow two different paths: chaos follows the onset of the cross of Saint Andrew (meniscus wave) occupying all of the diagonal or an unstable pattern in the form of an odd polygon.

Abbreviations

A_f	Forcing amplitude (mm)
A^+	Relationship between A_f and h ($A^+ = A_f / h$)
h	Fluid depth (mm)
H	Container height (mm)
l	Square container width (mm)
L_c	Container characteristic length (mm)
r_f	Forcing ratio $r_f = \omega_f / \omega_{max}$ imposed on the flow system
r_ω	Frequencies ratio $r_\omega = \omega_s / \omega_f$ associated with surface waves
N^*	New dimensionless number
St	Stokes number
We	Weber number
Γ	Filling ratio $\Gamma = L_c / h$
θ	Fluid temperature (°C)
λ^*	Dimensionless surface wavelength
ν	Kinematic viscosity (m^2/s)
ρ	Fluid density (kg/m^3)
σ	Surface tension (N/m)
ω_f	Forcing frequency (rd/s)
ω_{max}	Maximum forcing Frequency $\omega_{max} = 28.48$ rd/s
ω_s	Vibration frequency of free surface (rd/s)

1 Introduction

The formation of stationary waves on the free surface of a liquid subjected to a periodic vertical acceleration was first observed by Faraday [1]. He indicated that the frequency of the developed stationary wave is half of the frequency of the imposed external force.

[a] e-mail: r.guedifa@univ-boumerdes.dz (corresponding author)
[b] e-mail: ma.hachemi@univ-boumerdes.dz

Published online: 09 May 2022

Later, the results of Faraday were confirmed by Lord Rayleigh [2, 3], and Benjamin and Ursell [4], who realized the first linear stability analysis of the Faraday instability with the approximation of inviscid fluids. These authors expanded the flow in normal modes and showed that the equation of each mode corresponds to a Mathieu equation and they established the stability diagram.

Numerous experimental investigations have been conducted on the Faraday Instability (Ciliberto and Gollub [5], Douady and Fauve [6], Douady [7], Das and Hopfinger [8], Batson et al. [9], Rajchenbach et al. [10], Rajchenbach et al. [11]) who observed new patterns, such as super-lattices of squares (Tufillaro et al. [12]), octagonal or dodecahedral quasicrystals (Christiansen et al. [13], Edwards and Fauve [14]). Muller [15] observed triangular periodic patterns, not seen until that date.

In addition, Kudrolli et al. [16] obtained super-lattices of triangle using a periodic forcing of two frequencies. Kudrolli and Gollub [17] performed a parametric study of the patterns (squares, stripes and hexagons) depending on the viscosity and the forcing frequency. In particular, they studied spatio-temporal chaos in Faraday waves, whose existence had been previously reported in Ezerskii [18]. Binks et al. [19] examined the influence of filling ratio on the pattern formation. Lioubashevski et al. [20] discovered highly localized circular waves for the first time. Furthermore, Kityk et al. [21] used a quantitative measurement technique, operator light density, to evaluate the spatio-temporal Fourier spectra related to the instability of Faraday.

It is important to note that the majority of these experimental works used high forcing frequencies, $30 < f < 500\ Hz$. However, there exist a few works at low frequencies. Simonelli and Gollub [22] have conducted an experimental study to investigate the nonlinear interaction of two modes for $f = 20\ Hz$. Batson et al. [9] observed that meniscus waves decrease the interface peaks when the Faraday instability is triggered for $f > 10\ Hz$. Rajchenbach et al. [10] conducted an experimental study on Faraday waves with a forcing frequency ranging from 8 to 20 Hz. They reported the existence of 2D highly localized standing patterns of even and of odd symmetry. In another experimental investigation, Rajchenbach et al. [11] used containers of various shapes (rectangular, circular) with a forcing frequency in the range 7–11 Hz. They observed stars and polygons with other symmetries by varying the frequency and the amplitude of vibration.

Furthermore, many theoretical studies were inspired by the experimental study listed above. Kumar and Tuckerman [23] have generalized the study of the linear stability of Benjamin and Ursell [4] for viscous fluids. The results of Kumar and Tuckerman [23] were confirmed by the experiments of Bechhoefer et al. [24], and were used by Kumar [26] to determine the cases in which the response of the fluid to forcing frequency would be harmonic or sub-harmonic. Besson et al. [25] also extended the method of Kumar and Tuckerman [23] to two-frequencies forcing. Beyer and Friedrich [27] proposed another formulation of the viscous linear stability problem and another method for solving it. Weakly nonlinear approximations have been deduced by Zhang and Vinals [28], Chen and Vinals [29] and Skeldon and Guidoboni [30]. Porter et al. [31] have analyzed the different modes of instability using the theory of dynamical systems to generate the various patterns. Rucklidge and Silber [32] have proposed an approximation of quasi-crystals type in spatially periodic fields.

The Faraday instability in the nonlinear regime becomes very complex and therefore requires numerical solution. Simulations of the two-dimensional Faraday problem have been carried out (Chen and Wu [33], Chen [34], Murakami and Chikano [35], Valha et al. [36], Ubal et al. [37]).

Furthermore, Périnet et al. [38, 39] performed the first three-dimensional direct numerical simulation of this problem. They were able to reproduce the square and hexagonal patterns. Kahouadji et al. [40] presented three-dimensional numerical results on the Faraday instability in domains much larger than the critical wavelength in both square and cylindrical containers. Takagi and Matsumoto [41] reported the first numerical calculation of two-frequency forced Faraday waves.

Moreover, Ibrahim [42] presents a detailed overview of different problems of Faraday waves; the effect of viscosity and surface tension on the stability and response of the free surface.

Despite the fact that interfacial instabilities have been largely investigated experimentally and numerically in the past by numerous researchers for different working fluids and various container shapes, experimental studies of the forced surface waves for low forcing frequencies are rare, to the best of our knowledge. The main goal of our experimental work is to investigate the surface waves at low forcing frequencies, $3\ \text{Hz} < f < 5\ \text{Hz}$, and high forcing amplitudes, $3\ \text{mm} < A_f < 15\ \text{mm}$. We study the patterns generated by the meniscus waves, solitary waves and the onset of Faraday instability as well as to measuring the frequency and wavelength of interface response.

2 Experimental setup

We fill a container with sides of $a = 190$ mm with distilled water ($h \in [3, 20]$ mm). The container is mounted on a mobile plate driven by a sinusoidal and vertical movement with a forcing frequency (f) less than 5 Hz, and a range of forcing amplitude ($A_f \in [3, 15]$ mm), as shown in Fig. 1. The mobile plate is oscillated by a camshaft, which is driven by an electric motor (1500 tr/mn). A gear reducer (1/5) is used to decrease the rotational frequency to 5 Hz. The oscillation amplitudes are obtained by using various cams (3, 5, 10 and 15 mm). The forcing frequency is the same as that of the motor rotation frequency, which is controlled via an electric current variator.

A high-definition camera (60 fps) is used to determine the oscillation period and the size of the patterns. Note that more details on the wavelength measurement technique are given in "Appendix A."

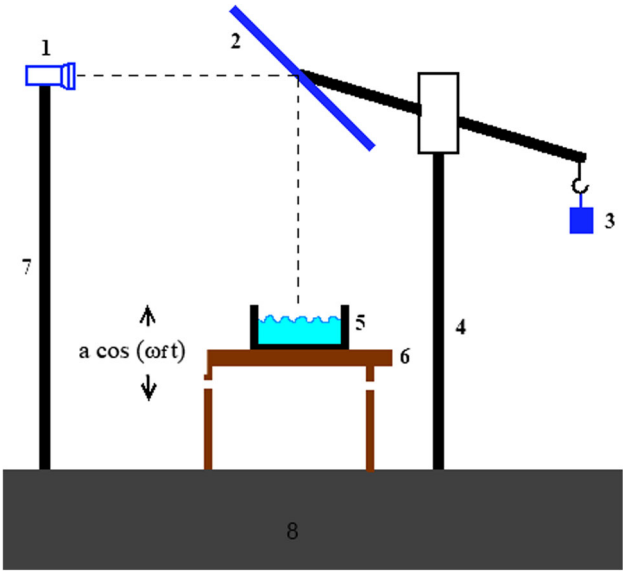

Fig. 1 Sketch of the experimental device. (1): Camera. (2): Mirror. (3): Counterweight. (4): Feet of the mirror. (5): Container. (6): Mobile plate/oscillating. (7): Camera feet. (8): Ground

3 Main results

We have filled the container with water up to a level of $h = 10$ mm. The water temperature is $\theta = 23.6$ °C, the forcing amplitude is $A_f = 5$ mm (forcing ratio $A^+ = A_f/h = 1/2$) and the forcing frequency is $f = 4.4$ Hz (with a maximum frequency $f_{max} = 5$ Hz and a forcing ratio $r_f = f / f_{max} = 0.88$).

The surface waves are generated by the propagation of meniscus waves, which agrees very well with the experimental work of Batson et al. [9]. In our experimental work, the initial transitional modes last a maximum of 180 s before the steady regime is established. Once a steady regime is reached (after 60 s), the gravity waves form a square pattern of wavelength $\lambda_s = 41.23$ mm which oscillates with frequency $f_s = 5.2$ Hz, as illustrated in Fig. 2.

We report the dimensionless wavelength $\lambda^* = \lambda_s/a$ and frequency response ratio $r_\omega = f_s/f$. We obtain in this case: $\lambda^* = 0.37$ and $r_\omega = 1.04$. We use another time variable, which is the oscillation period of the interface $T_s = 1 / f_s$. It can be seen that small waves occur in the middle of the domain. There are solitary waves of wavelength $\lambda_{Soli} = 1.52$ mm, which have the same vibrational frequency than the surface waves, and a low amplitude which decreases away from the principal peaks of the observed structure, as shown in Fig. 2e.

Noteworthy is that there are other experimental works that have used water as the working fluid and compared the measured wavelengths with classic gravity-capillary wavelength. However, in our case that the vibrational frequency is too small i.e., <5 Hz, making it rather difficult.

3.1 Dependence of the pattern on the forcing frequency

We increase the imposed forcing frequency in order to observe the evolution of the pattern and its response frequency.

We obtain a succession of steady patterns, which are shown in Fig. 3.

Furthermore, we have highlighted a new dimensionless number, N^*, that characterizes this forcing-dissipation duel combining between the Stokes number, St, and the Weber number, We "Appendix B". This number, N^*, is significant because it represents a ratio between kinetic energy and viscous dissipation divided on the ratio between potential energy and surface tension, which is defined as:

$$N* = \mathrm{St/We} = [\omega \cdot h^2/\nu] \cdot [\sigma/(\rho \cdot V^2 \cdot h)] = \omega \cdot [h/L_c]^2 \cdot \left[L_c^2/\nu\right] \cdot \left[L_c \cdot \sigma/\left(\rho \cdot A_f^2 \cdot \omega^2 \cdot h \cdot L_c\right)\right].$$

$$N* = L_c\left[\Gamma/\left(\omega \cdot A_f^2\right)\right] \cdot [\sigma/(\rho \cdot \nu)].$$

The comparative analysis of the developments of frequency ratio r_ω and the wavelength λ^* in function of the forcing ratio r_f and the dimensionless number N^* is similar because it varies quasi-constant on the intervals explored, as shown in Fig. 4.

The number $N*$ is inversely proportional to the forcing frequency, as illustrated in formula. The first three points do not follow the curve because they characterize higher forcing frequencies, which are accompanied by an ejection of micro drops that break the flow.

The onset of the Faraday instability increases the wavelength λ^**up to* and it decreases the frequency in free surface until half forcing frequency.

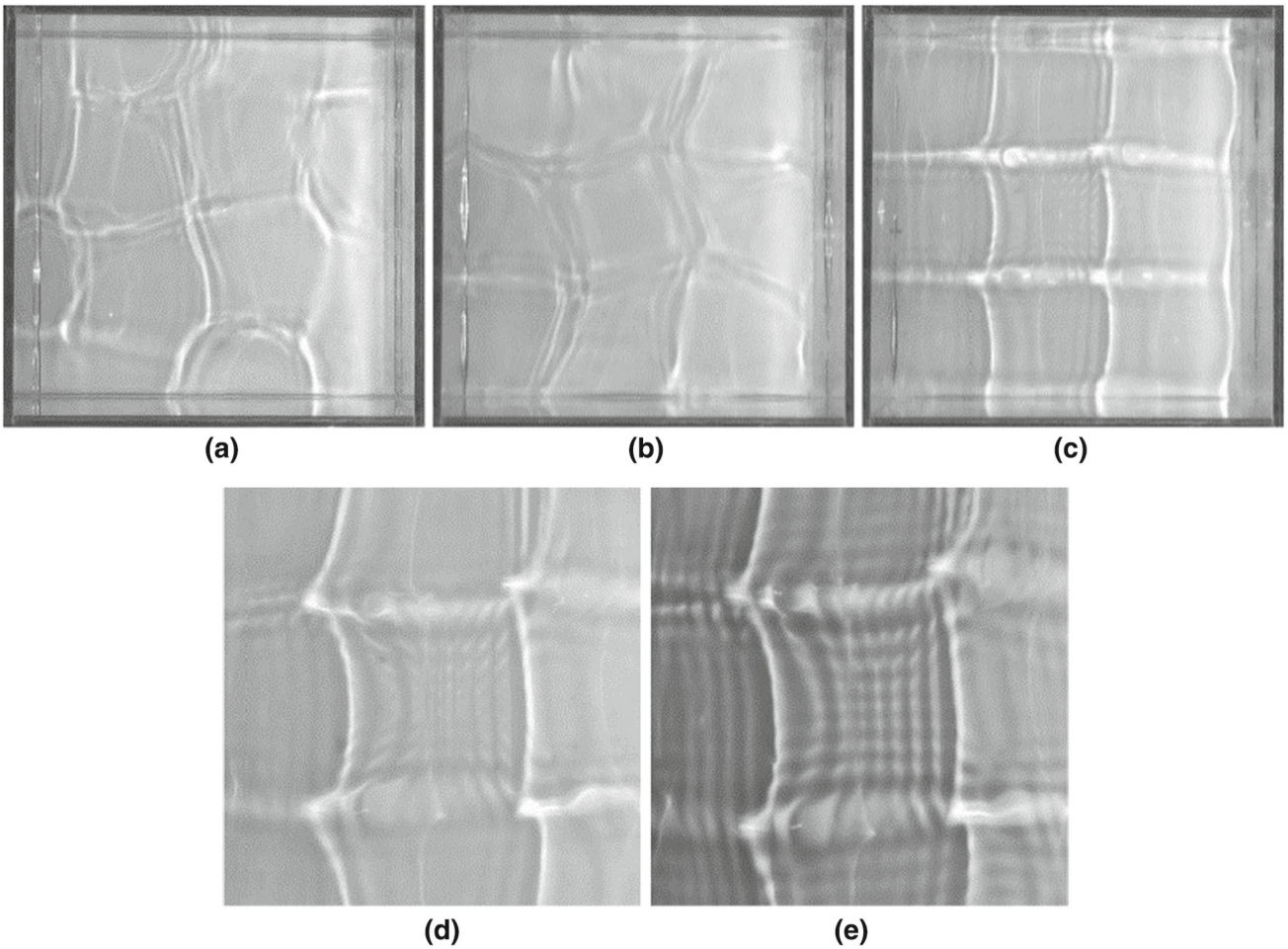

Fig. 2 Temporal and structural evolution of interfacial motion: onset of the Faraday instability in a cubic cell filled with water for the conditions ($h = 10$ mm, $A^+ = 1/2$ and$f = 4.4$ Hz). **a**: transient regime $t = 25.40$ s. **b**: transient regime $t = 58.20$ s. **c**: Regime established $t = 65.10$ s. **d**: Focus on the central area of the measuring cell $t = 65.40$ s. **e**: Saturation in gray of picture **f** $t = 65.40$ s

3.2 Influence of forcing amplitude

For each test, we have fixed the same filling ratio Γ and we have changed the other two parameters: forcing amplitude A_f ($A^+ = A_f/h$) and the forcing frequency $\omega_f(r_f = \omega_f/\omega_{max})$. For each forcing frequency, we have defined the surface frequency $\omega_s(r_\omega = \omega_s/\omega_f)$ and the surface wavelength λ_s ($\lambda^* = \lambda_s/L_c$).

From Fig. 5, it can be seen that the gravity waves are characterized by the patterns of three or four order (triangles or squares) in which the periods are easy to determine. The evolution of the flow as the forcing frequency is varied to a dominant mode corresponds to rotation of the patterns in the container that take the form of complex patterns such as hexagons, octagons or equilateral triangles.

For a forcing frequency $f = 4.3$ Hz thick stripes appear, which alternately form a square oriented diagonally with respect to the square container, and a Saint Andrew's cross. The temporal response in this case is subharmonic, as illustrated in Fig. 6.

For low forcing amplitudes $A_f < h$, the wavelength varies weakly over the range $0.3 < \lambda^* < 0.5$. For fixed A^+, the frequency at which waves first appear is observed for a low forcing frequency $f = 3.6$ Hz ($r_f = 0.72$), as shown in Fig. 7.

For higher forcing amplitudes, the frequency at which waves first appear is quite low.

3.3 Influence of the geometrical factor: filling ratio

Consider a low forcing amplitude $A_f = 5$ mm in order to observe the Faraday instability and the change of regimes and then to compare the results with the first case ($\Gamma = 1/19$, $A^+ = 1/2$), as shown in Figs. 8 and 9.

Due to the fluid depth, which is more important compared to the previous experiment, the patterns related to the periodic structure lose the symmetry (unsteady waves). The center of symmetry of the considered pattern moves horizontally and there are different heights of peaks, one to the other, as can be seen in Fig. 9.

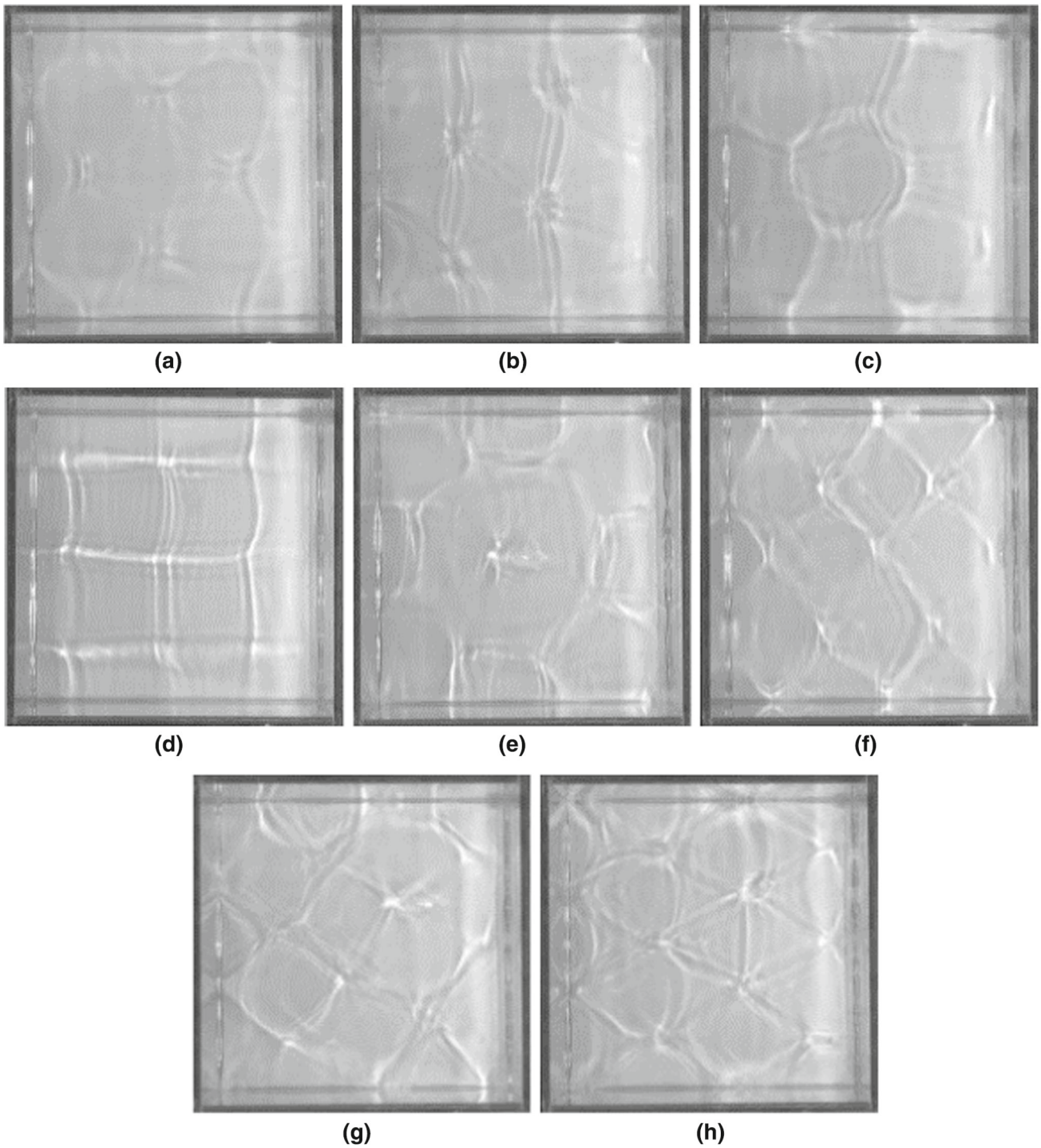

Fig. 3 Dependence of the pattern on the forcing frequency ($h = 10$ mm and $A^{+} = 1/2$). **a**: square-diamond $f = 4.3$ Hz, $\theta = 24.0$ °C, $r_\omega = 1.07$. **b**: equilateral triangles $f = 4.35$ Hz, $\theta = 24.0$ °C, $r_\omega = 1.06$. **c**: octagon–square $f = 4.4$ Hz, $\theta = 23.6$ °C, $r_\omega = 1.04$. **d**: square Super-lattices $f = 4.45$ Hz, $\theta = 23.6$ °C, $r_\omega = 0.89$. **e**: Octagon centered $f = 4.7$ Hz, $\theta = 23.6$ °C, $r_\omega = 0.84$. **f**: diamonds $f = 4.8$ Hz, $\theta = 23.6$ °C, $r_\omega = 1.15$. **g**: squares $f = 4.9$ Hz, $\theta = 23.6$ °C, $r_\omega = 0.94$. **h**: equilateral triangles Super-lattice$f = 5$ Hz, $\theta = 23.6$ °C, $r_\omega = 1.10$

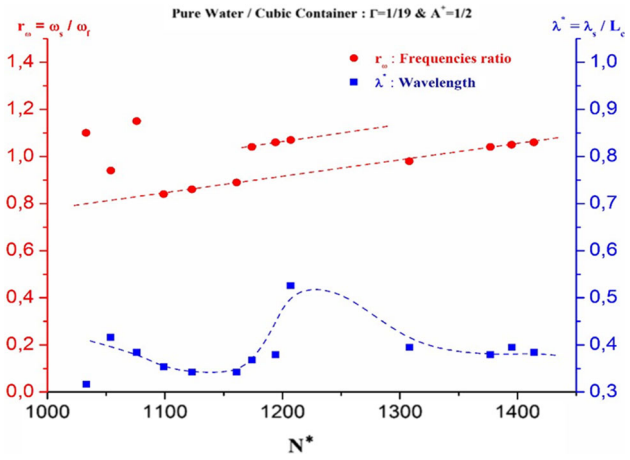

Fig. 4 Variation in the wavelength λ^* and the frequency ratio r_ω according to N^* under the following conditions ($h = 10$ mm and $A^+ = 1/2$)

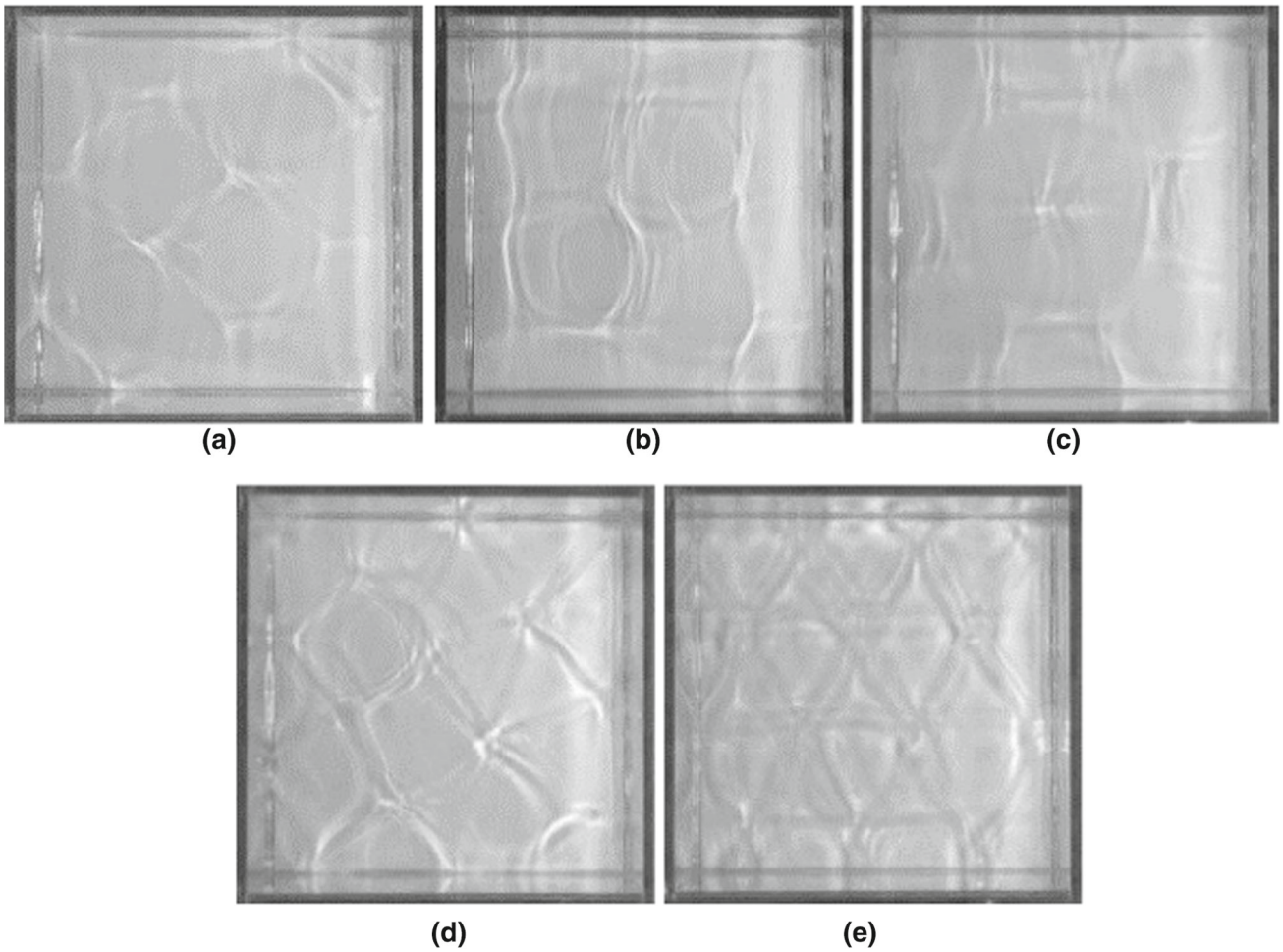

Fig. 5 Evolution of the pattern as a function of the forcing frequency f ($h = 10$ mm and $A^+ = 3/10$). **a**: squares $f = 4.4$ Hz, $\theta = 24.4$ °C, $r_\omega = 1.04$. **b**: diamond $f = 4.5$ Hz, $\theta = 25.2$ °C, $r_\omega = 1.02$. **c**: Octagon centered $f = 4.7$ Hz, $\theta = 25.2$ °C, $r_\omega = 0.98$. **d**: Octagon–square $f = 4.9$ Hz, $\theta = 24.6$ °C, $r_\omega = 1.13$. **e**: equilateral triangles $f = 4.95$ Hz, $\theta = 24.6$ °C, $r_\omega = 1.11$

When the upward jet splits into droplets, the wave amplitude can be about 2 times the liquid mean depth, disrupting the surface wave and ending the steady regime as reported by Rajchenbach et al. [11].

Figure 10 shows the variation curve of wavelength λ^* as function of the ratio of forcing amplitude r_f. It is clearly observed that the wavelengths associated with the capillary regime are shorter compared to the gravity regime.

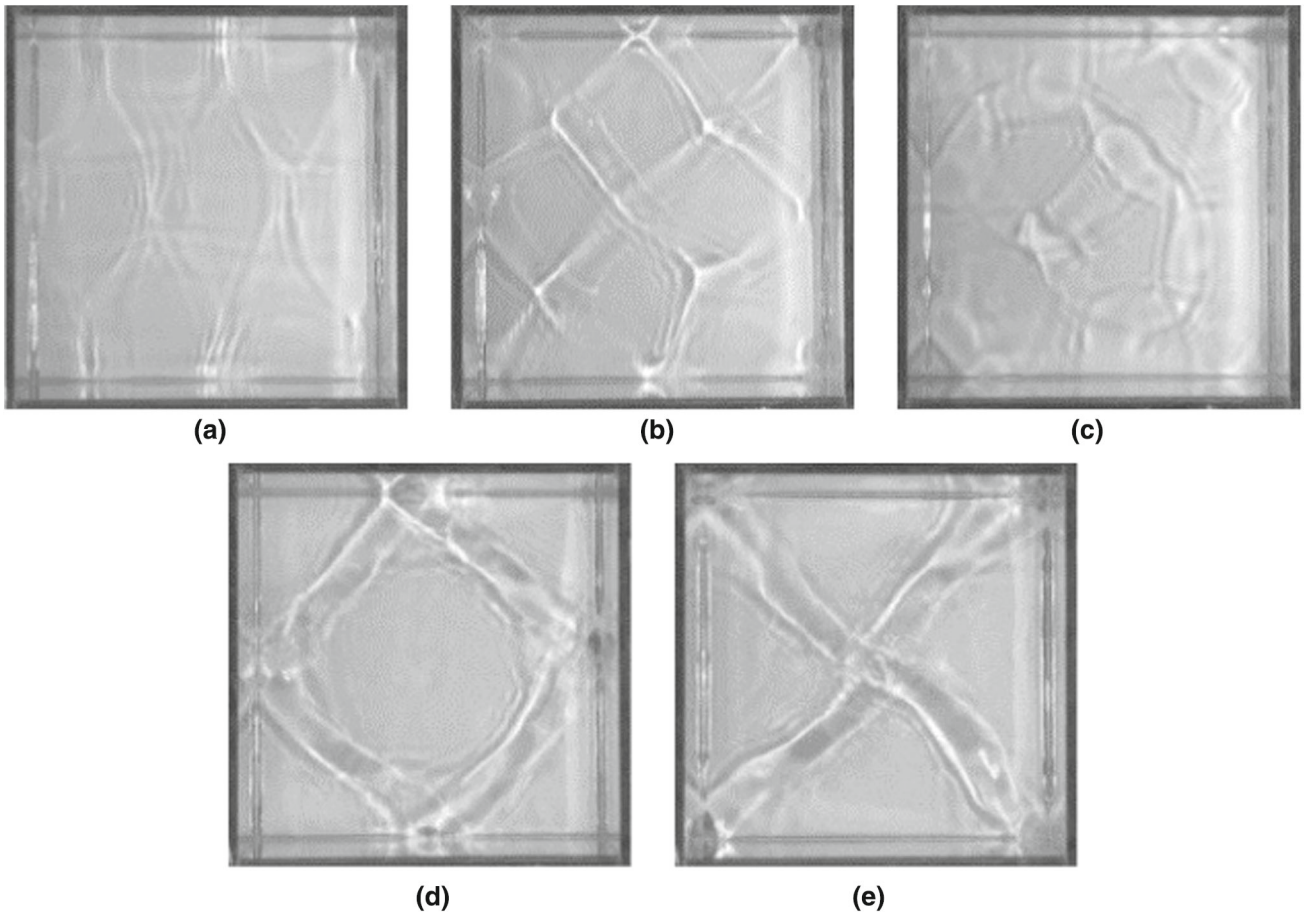

Fig. 6 Evolution of the pattern as a function of the forcing frequency f ($h = 10$ mm and $A^+ = 1$). **a**: diamond $f = 4$ Hz, $\theta = 22.2$ °C, $r_\omega = 1.15$. **b**: squares $f = 4.1$ Hz, $\theta = 22.2$ °C, $r_\omega = 1.12$. **c**: pentagon $f = 4.2$ Hz, $\theta = 22.2$ °C, $r_\omega = 1.09$. **d**: Saint Andrew's cross $f = 4.4$ Hz, $\theta = 22.2$ °C, $r_\omega = 0.52$, $t = t_0 + T_s / 4$. **e**: Saint Andrew's cross $f = 4.4$ Hz, $\theta = 22.2$ °C, $r_\omega = 0.52$, $t = t_0 + 3T_s / 4$

Fig. 7 Evolution of the wavelength λ^* as function of the forcing frequency f and amplitude A^+ for $h = 10$ mm

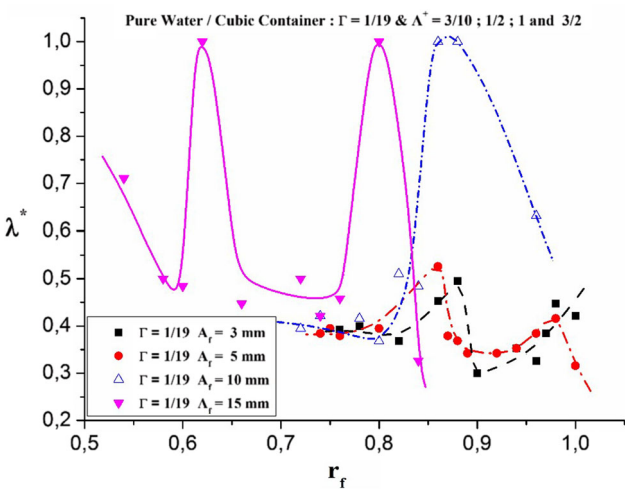

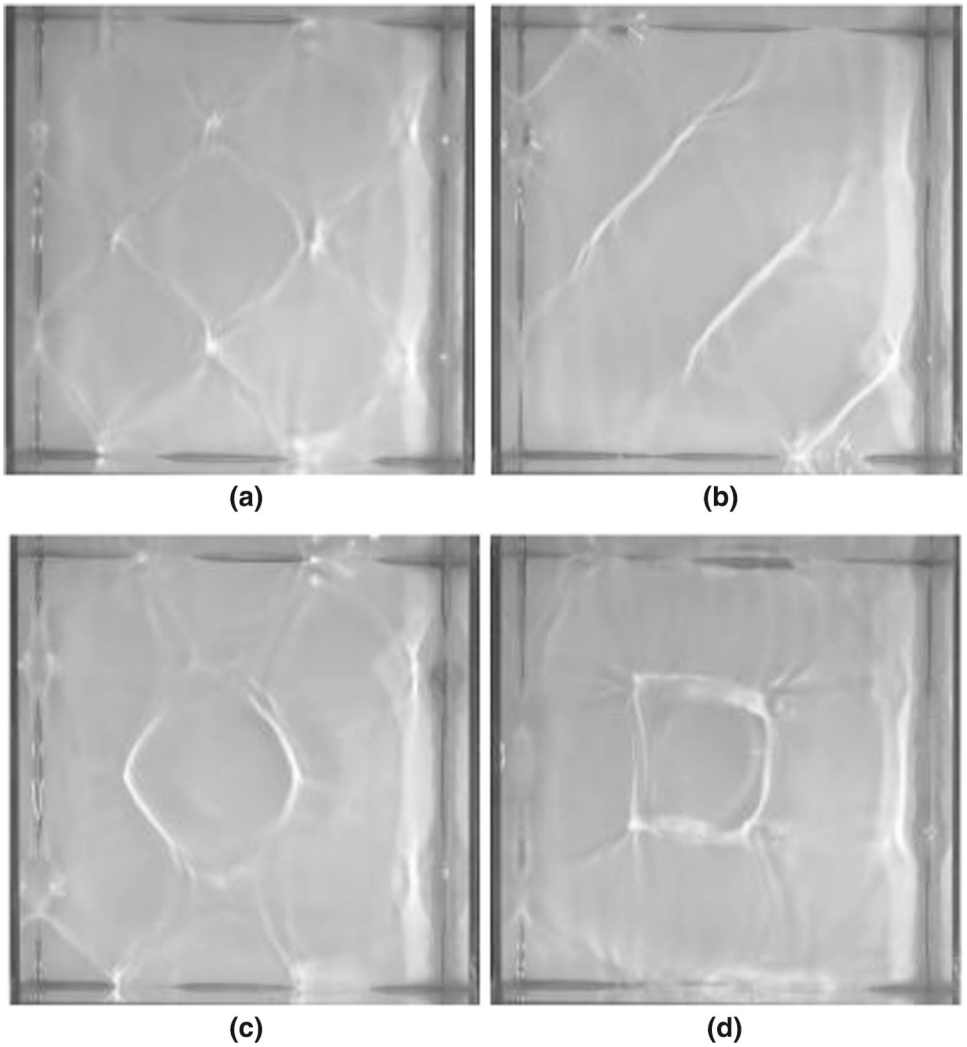

Fig. 8 Structural evolution of the interfacial movement as function of the forcing frequency ω_f (Γ = 3/38 and $A^+ = 1/3$). **a**: Structure in diamond-squares symmetric r_f = 0.90, θ = 22.0 °C, r_ω = 0.88, λ^* = 0.49. **b**: Structure in diamond-squares symmetric r_f = 0.90, θ = 22.4 °C, r_ω = 1.02, λ^* = 0.50. **c**: Structure in octagon–square r_f = 0.92, θ = 22.4 °C, r_ω = 1.00, λ^* = 0.43. **d**: Structure in squares super-lattice r_f = 0.94, θ = 22.4 °C, r_ω = 0.98, λ^* = 0.32

The filling ratio is a factor that affects the appearance of the interface's vibration regimes. At a filling ratio Γ = 1/38, the system is placed under the conditions of observation of the capillary regime for the forcing amplitudes lower than three times of the filling height.

4 Concluding remarks

In this paper, we have investigated experimentally the various patterns formation in forced surface waves by the measure of wavelength and interface frequency. The description and analysis of the salient results give the following comments:

- For the low forcing amplitudes, there is a weak variation of the wavelength.
- When the forcing amplitude increases, the occurrence frequency related to the first wave appears to be quite low. However, The Faraday instability is better observed for large forcing amplitudes for a given filling ratio.
- The filling ratio has a great influence on the emergence of interface's vibration regimes. For a low filling ratio Γ = 1/38 (h = 5 mm), the condition of observation of the capillary regime is realized for the forcing amplitudes less than three times of the filling height ($A + < 3$). However, the increase in the filling ratio accelerates the emergence of gravity regime that will give way to a chaotic regime if we continue to increase the imposed forcing amplitude.
- The cubic cell favors the appearance of patterns in square or triangular shapes compared to other of higher order: hexagons, heptagons, octagons, decagons, dodecagons, etc.

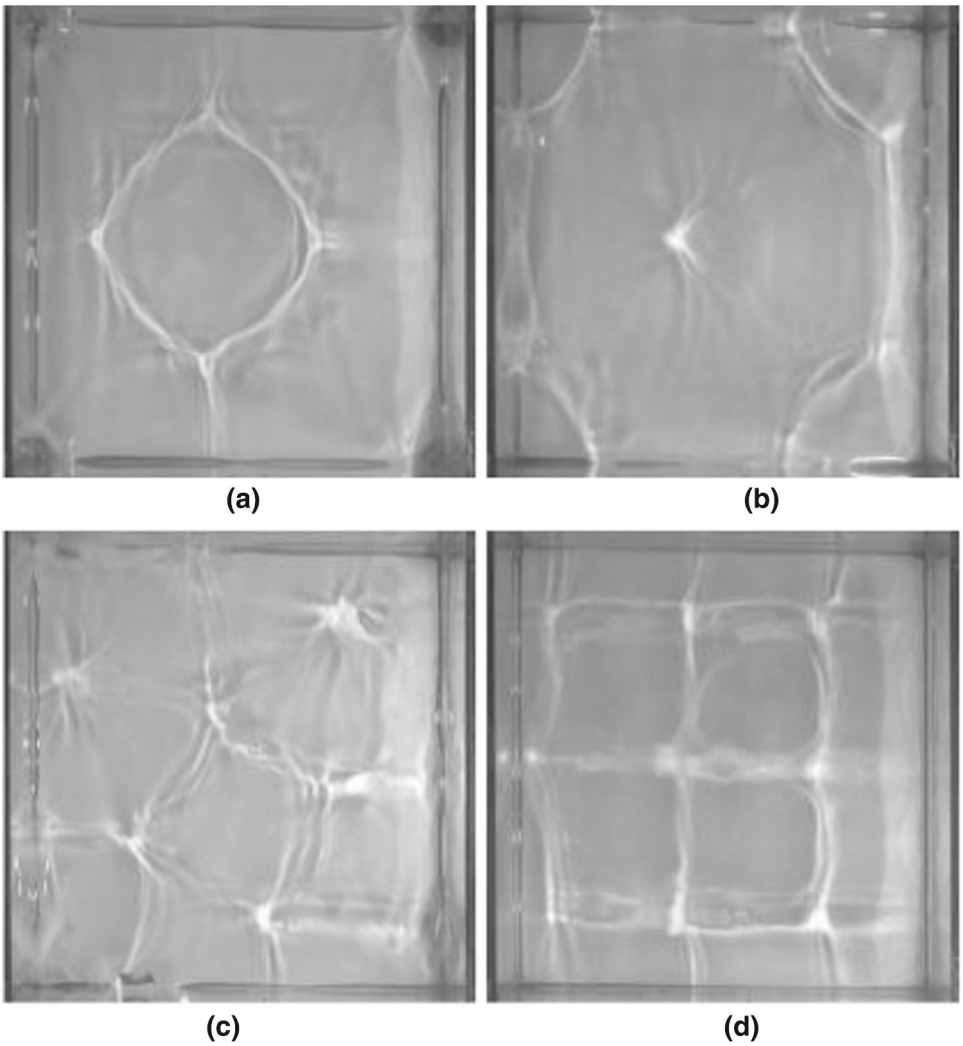

Fig. 9 Structural evolution of the interfacial movement depending on the forcing frequency ω_f (Γ = 2/19 and A^+ = 1/4). **a**: Structure in diamond-squares symmetric r_f = 0.78, θ = 22.4 °C, r_ω = 1.01, λ^* = 0.51, $t = t_0 + T_s / 4$. **b**: structure in equilateral triangles r_f = 0.78, θ = 22.4 °C, r_ω = 1.01, λ^* = 0.52, $t = t_0 + 3T_s / 4$. **c**: structure in octagon–square r_f = 0.80, θ = 22.6 °C, r_ω = 0.86, λ^* = 0.53. **d**: structure in squares super-lattice r_f = 1.00, θ = 22.6 °C, r_ω = 1.10, λ^* = 0.30

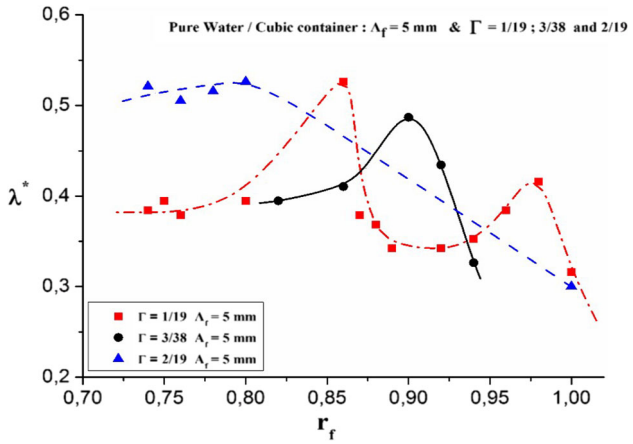

Fig. 10 Evolution of wavelength λ^* as function of the ratio of forcing amplitude r_f

Acknowledgements We acknowledge Dr Lalaoua Adel for fruitful discussions and his encouragement.

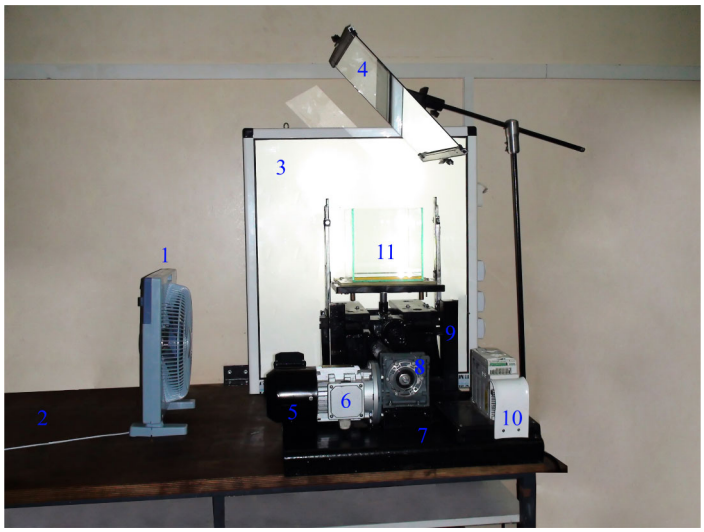

Fig. 11 Experimental devices

(1): Fan.
(2): Fixed table.
(3): Lighting panel.
(4): Viewing mirror.
(5): Fan.
(6): Electric motor.
(7): Carrier table.
(8): Speed reducer.
(9): Fixed frame.
(10): Current variator.
(11): Cubic cell.

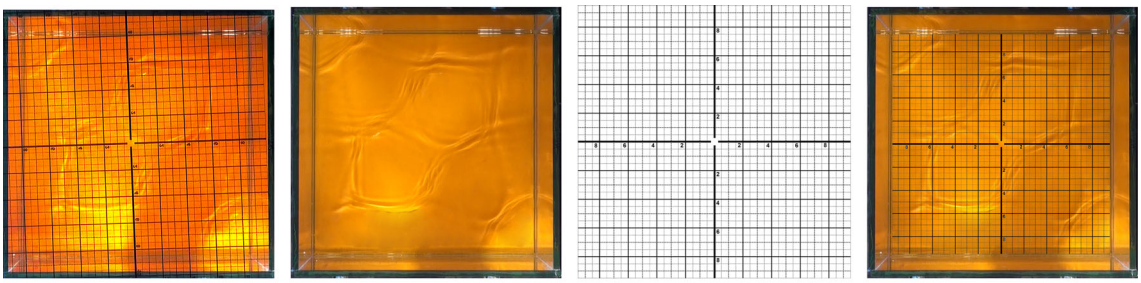

Fig. 12 Image scaling

Appendix A: The measurement technique of wavelength

1/ Camera positioning As our phenomenon has different shapes of patterns that typically characterize a given flow vibrational state, one is compelled to take pictures from the top of the flow system (Fig. 11).

However, the problem is to have a technique which ensures the perpendicularity of the camera with respect to the free surface and to avoid the projection of the shadow of the camera on this surface coming from the reflection of the internal light of the room. Under these conditions, an optical technique based on mirror transmission is used. The mirror used is square ($l = 500$ mm) mounted on an arm and fixed by a pivot pin. The angle of inclination is (45°). This is held fixed by a counterweight to prevent any movement of the mirror during the experiment. Then, the height of the camera is adjusted so that its axis is centered in the middle of the mirror as well as the container. The two load-bearing feet must be far from the test table in order to avoid the problem of transmission of vibrations from the table fixed to the ground.

2/ Registration To visualize the phenomenon of instability, we choose to operate in video scenes because of the very fast speed of the movement. In our experiments, we have used a Sony HandyCam HDR-XR520 camera.

3/ Image extraction method To carry out the photometric study, a computer station is available to carry out the acquisition and processing of data.

The computer processes 60 frames per second (1920*1080 pixels), where the size of the image on disk will be 7.91 Mb. Generally, we limit ourselves to a duration that does not exceed 10 s corresponding to a maximum of 600 images for each test.

4/ Image scaling First of all, we tried to take the video scenes with transparent millimeter paper. This choice posed several problems for us such as the reflection on the surface of the millimeter paper and the volume of air present in the container which led to vibrations and shifting of the millimeter paper, as can be seen in Fig. 12a.

In order to determine the wavelength, we relied on the method of merging two images using photographic processing software. Our container has an internal length of 190 mm (for an image captured in 1920*1080 pixels (Fig. 12b) the length will be 1026 pixels). Then the transparent millimeter paper of dimension (square, side length 190 mm) will be resized to (1026*1026 pixels Fig. 12c). The image obtained (Fig. 12d) after merging two images (Fig. 12b, c) has a better quality compared to the first (Fig. 12a).

Appendix B: Estimation of errors

The new dimensionless number is defined as:

$$N^* = \frac{St}{We} = \left(\frac{\omega h^2}{\nu}\right)\left(\frac{\sigma}{\rho V^2 h}\right) = \omega\left(\frac{h}{L_c}\right)^2 \frac{L_c^2}{\nu} \frac{L_c \sigma}{\rho A_f^2 \omega^2 h L_c} = \frac{\Gamma L_c}{A_f^2 \omega} \frac{\sigma}{\rho \nu}.$$

Taking the corresponding logarithm:

$$\mathrm{Log} N^* = \mathrm{Log}\, St - \mathrm{Log}\, We = \mathrm{Log}\,\Gamma + \mathrm{Log} L_c - 2\mathrm{Log} A_f - \mathrm{Log}\,\omega - \mathrm{Log}\,\rho + (\mathrm{Log}\,\sigma - \mathrm{Log}\nu)$$

Let's derive the previous expression:

$$\frac{\mathrm{d}N^*}{N^*} = \frac{\mathrm{d}\Gamma}{\Gamma} + \frac{\mathrm{d}L_c}{L_c} - 2\frac{\mathrm{d}A_f}{A_f} - \frac{\mathrm{d}\omega}{\omega} - \frac{\mathrm{d}\rho}{\rho} + \left(\frac{\mathrm{d}\sigma}{\sigma} - \frac{\mathrm{d}\nu}{\nu}\right)$$

In our case, the amplitude, forcing frequency, filling rate, container diameter and density parameters are known and fixed at the start. However, it remains to evaluate the error committed if the surface tension and the kinematic viscosity must be known. Under these conditions, we obtain the following result:

$$\frac{\Delta N^*}{N^*} = \frac{\Delta\Gamma}{\Gamma} + \frac{\Delta L_c}{L_c} + 2\frac{\Delta A_f}{A_f} + \frac{\Delta\omega}{\omega} + \frac{\Delta\rho}{\rho} + \left(\frac{\Delta\sigma}{\sigma} + \frac{\Delta\nu}{\nu}\right)$$

In practice, the errors are evaluated as:

$$\frac{\Delta\Gamma}{\Gamma} = \frac{\Delta \mathrm{h}}{h} + \frac{\Delta L_c}{L_c} = 0.75\%,\ \frac{\Delta L_c}{L_c} = 0.25\%,\ \frac{\Delta\rho}{\rho} = 1\%,\ \frac{\Delta h}{h} = 0.5\% \text{ and } \frac{\Delta A_f}{A_f} = 1\%.$$

By definition, the pulsation ω is linked to the excitation frequency ($\mathbb{N}_t$) such that:

$$\omega = 2\pi \mathbb{N}_t$$

Hence, the error is given by the following relation:

$$\frac{\Delta\omega}{\omega} = \frac{\Delta \mathbb{N}_t}{\mathbb{N}_t} = 0.2\%$$

The defined errors are estimated, respectively, at:

$$\Delta\nu/\nu = 1.1\% \, and \, \Delta\sigma/\sigma = 1.2\%$$

So, we find a total error:

$$\frac{\Delta N^*}{N^*} = 7\%$$

We note that the errors relating to the numbers of Stokes and Weber are, respectively

$$\frac{\Delta \mathrm{St}}{\mathrm{St}} = 2\% et \frac{\Delta \mathrm{We}}{\mathrm{We}} = 5\%$$

References

1. M. Faraday, Philos. Trans. R. Soc. London **121**, 299–340 (1831). http://www.jstor.org/stable/107936
2. L. Rayleigh, Philos. Mag. **15**, 229–235 (1883). https://doi.org/10.1080/14786448308627342
3. L. Rayleigh, Philos. Mag. **16**, 50–58 (1883). https://doi.org/10.1080/14786448308627392
4. T.B. Benjamin, F. Ursell, Proc. R. Soc. Lond. **225**, 505–515 (1954). https://doi.org/10.1098/rspa.1954.0218
5. S. Ciliberto, J.P. Gollub, J. Fluid Mech. **158**, 381–398 (1985). https://doi.org/10.1017/S0022112085002701
6. S. Douady, S. Fauve, Europhys. Lett. **6**, 221–226 (1988). https://doi.org/10.1209/0295-5075/6/3/006
7. S. Douady, J. Fluid Mech. **221**, 383–409 (1990). https://doi.org/10.1017/S0022112090003603
8. S.P. Das, E.J. Hopfinger, J. Fluid Mech. **599**, 205–228 (2008). https://doi.org/10.1017/S0022112008000165
9. W. Batson, F. Zoueshtiagh, R. Narayanan, J. Fluid Mech. **729**, 496–523 (2013). https://doi.org/10.1017/jfm.2013.324
10. J. Rajchenbach, A. Leroux, D. Clamond, Phys. Rev. Lett. **107**, 024502 (2011). https://doi.org/10.1103/PhysRevLett.107.024502
11. J. Rajchenbach, D. Clamond, A. Leroux, Phys. Rev. Lett. **110**, 094502 (2013). https://doi.org/10.1103/PhysRevLett.110.094502
12. N.B. Tufillaro, R. Ramshankar, J.P. Gollub, Phys. Rev. Lett. **62**, 422–425 (1989). https://doi.org/10.1103/PhysRevLett.62.422
13. B. Christiansen, P. Alstrom, M.T. Levinsen, Phys. Rev. Lett. **68**, 2157–2161 (1992). https://doi.org/10.1017/S0022112095002722
14. W.S. Edwards, S. Fauve, Phys. Rev. E **47**(2), R788–R791 (1993). https://doi.org/10.1103/PhysRevE.47.R788
15. H.W. Muller, Phys. Rev. Lett. **71**, 3287–3290 (1993). https://doi.org/10.1103/PhysRevLett.71.3287
16. A. Kudrolli, B. Pier, J. P. Gollub, Physica D, **123**, 99–111 (1998). https://doi.org/10.1016/S0167-2789(98)00115-8
17. A. Kudrolli, J. P. Gollub, Physica D, **97**, 133–154 (1996). https://doi.org/10.1016/0167-2789(96)00099-1

18. A. B. Ezerskii, M. I. Rabinovich, V. P. Reutov, I. M. Starobinets, Transl. Sov. Phys. JETP **64**, 1228–1236 (1986). http://jetp.ac.ru/cgi-bin/dn/e_064_06_1228.pdf
19. D. Binks, M.T. Westra, W. Van Der Water, Phys. Rev. Lett. **79**, 5010–5013 (1997). https://doi.org/10.1103/PhysRevLett.79.5010
20. O. Lioubashevski, H. Arbell, J. Fineberg, Phys. Rev. Lett. **76**, 3959–3962 (1996). https://doi.org/10.1103/PhysRevLett.76.3959
21. A.V. Kityk, J. Embs, V.V. Mekhonoshin, C. Wagner, Phys. Rev. E **72**, 036209 (2005). https://doi.org/10.1103/PhysRevE.72.036209
22. F. Simonelli, J.P. Gollub, J. Fluid Mech. **199**, 471–494 (1989). https://doi.org/10.1017/S0022112089000443
23. K. Kumar, L.S. Tuckerman, J. Fluid Mech. **279**, 49–68 (1994). https://doi.org/10.1017/S0022112094003812
24. J. Bechhoefer, V. Ego, S. Manneville, B. Johnson, J. Fluid Mech. **288**, 325–350 (1995). https://doi.org/10.1017/S0022112095001169
25. T. Besson, W.S. Edwards, L.S. Tuckerman, Phys. Rev. E **54**, 507–513 (1996). https://doi.org/10.1103/PhysRevE.54.507
26. K. Kumar, Proc. R. Soc. Lond. **452**, 1113–1126 (1996). https://doi.org/10.1098/rspa.1996.0056
27. J. Beyer, R. Friedrich, Phys. Rev. E **51**, 1162–1168 (1995). https://doi.org/10.1103/PhysRevE.51.1162
28. W. Zhang, J. Vinals, J. Fluid Mech. **336**, 301–330 (1997). https://doi.org/10.1017/S0022112096004764
29. P. Chen, J. Vinals, Phys. Rev. E **60**, 559–570 (1999). https://doi.org/10.1103/PhysRevE.60.559
30. A.C. Skeldon, G. Guidoboni, SIAM J. Appl. Math. **67**, 1064–1100 (2007). https://doi.org/10.1137/050639223
31. J. Porter, C.M. Topaz, M. Silber, Phys. Rev. Lett. **93**, 034502 (2004). https://doi.org/10.1103/PhysRevLett.93.034502
32. A.M. Rucklidge, M. Silber, SIAM J. Appl. Dyn. Syst. **8**, 298–347 (2009). https://doi.org/10.1137/080719066
33. P. Chen, K.A. Wu, Phys. Rev. Lett. **85**, 3813–3816 (2000). https://doi.org/10.1103/PhysRevLett.85.3813
34. P. Chen, Phys. Rev. E **65**, 036308 (2002). https://doi.org/10.1103/PhysRevE.65.036308
35. Y. Murakami, K. Chikano, Phys. Fluids **13**, 65–74 (2001). https://doi.org/10.1063/1.1327592
36. J. Valha, J.S. Lewis, J. Kubie, Int. J. Numer. Methods Fluids **40**, 697–721 (2002). https://doi.org/10.1002/fld.370
37. S. Ubal, M.D. Giavedoni, F.A. Saita, Phys. Fluids **15**, 3099–3113 (2003). https://doi.org/10.1063/1.1601220
38. N. Périnet, D. Juric, L.S. Tuckerman, J. Fluid Mech. **635**, 1–26 (2009). https://doi.org/10.1017/S0022112009007551
39. N. Périnet, D. Juric, L.S. Tuckerman, Phys. Rev. Lett. **109**, 164501(5) (2012). https://doi.org/10.1103/PhysRevLett.109.164501
40. L. Kahouadji, N. Périnet, L. S. Tuckerman, S. Shin, J. Chergui, D. Juric, J. Fluid Mech., **772**, R2 (2015) https://doi.org/10.1017/jfm.2015.213
41. K. Takagi, T. Matsumoto, Phys. Fluids **27**, 032108 (2015). https://doi.org/10.1063/1.4915340
42. R.A. Ibrahim, ASME J. Fluids Eng **137**(9), 090801 (52) (2015). https://doi.org/10.1115/1.4029544